Gouy's Phase Anomaly in Electron Waves Produced by Strong-Field Ionization

Simon Brennecke, Nicolas Eicke, and Manfred Lein
Leibniz Universität Hannover, Institut für Theoretische Physik, Appelstraße 2, 30167 Hannover, Germany

Ionization of atoms by strong laser fields produces photoelectron momentum distributions that exhibit modulations due to the interference of outgoing electron trajectories. For a faithful modeling, it is essential to include previously overlooked phase shifts occurring when trajectories pass through focal points. Such phase shifts are known as Gouy's phase anomaly in optics or as Maslov phases in semiclassical theory. Because of Coulomb focusing in three dimensions, one out of two trajectories in photoelectron holography goes through a focal point as it crosses the symmetry axis in momentum space. In addition, there exist observable Maslov phases already in two dimensions. Clustering algorithms enable us to implement a semiclassical model with the correct preexponential factor that affects both the weight and the phase of each trajectory. We also derive a simple rule to relate two-dimensional and three-dimensional models for linear polarization. It explains the shifted interference fringes and weaker high-energy yield in three dimensions. The results are in excellent agreement with solutions of the time-dependent Schrödinger equation.

The π phase shift of an electromagnetic wave as it passes through a focus is an astonishing effect. Even though it was already observed by Gouy [1] more than 100 years ago, recent advances in laser technology have shone new light on Gouy's phase [2–5]. Analogous phenomena have also been found in other types of waves such as acoustic waves [6], standing microwaves [7], phonon-polariton wave packets [8], and matter waves [9–11]. While a rigorous derivation of the phase jump is nontrivial, an intuitive picture is as follows. In a trajectory description, the passage of a wave through a focus means that the spatial extension of a bunch of trajectories (such as the spot size formed by geometric rays) goes through zero. If this spatial extension is defined with sign, there is a sign change at the focus. Wave amplitudes are inversely proportional to the square root of the interval size, so a sign change of a one-dimensional interval length leads to a $\pm\pi/2$ phase shift of the wave. The well-known optical Gouy phase of π arises because a light beam is typically focused in two variables: A two-dimensional area is focused to a point.

In the present work, we demonstrate that Gouy's phase anomaly appears in electron wave packets produced by strong-field ionization, leading to a significant imprint on interference structures in photoelectron momentum distributions (PMDs). Strong-field ionization may be viewed as a two-step process consisting of (i) release of an electron from the target and (ii) acceleration of the electron by the electromagnetic field in the presence of the potential of the parent ion [12,13]. Depending on the system geometry, different parts of the emitted wave packets are mapped to the same final momentum, creating interference structures [14–18]. As the positions of the interference fringes are determined by the phase difference between the wave

packets, the emerging PMD may be viewed as a "phasometer." For linearly polarized laser pulses, the PMDs are dominated by photoelectron holography [16,19–23] that may be explained by the interference of a "signal" wave that is scattered upon return to the parent ion and a nonscattered "reference" wave [24,25]. In full dimensionality (3D), Coulomb focusing makes rescattering wave packets pass through a focal point [26] and, as we show, it causes the appearance of Gouy's phase shift. This happens not only in linear polarization but also in other waveforms that give rise to rescattering. Because Coulomb focusing acts in 1 degree of freedom, it causes $\pi/2$ phase shifts, no matter whether the system possesses cylindrical symmetry or not. It explains why PMDs obtained by numerical solution of the time-dependent Schrödinger equation (TDSE) in full dimensionality (3D) agree well with experimental data [16,20], but PMDs obtained in reduced dimensionality (2D) are unable to reproduce quantitatively the fringe positions and heights seen in experiments [21]. Thus, it turns out that strong-field ionization is an ideal setup for observation of focal-point phases as it generates the fundamental value of $\pi/2$ and, without extra effort, it provides the interference with a reference trajectory.

In order to provide an illustrative picture in terms of classical trajectories, several attempts were undertaken to describe PMDs in the presence of ionic potentials semiclassically. The resulting models are able to explain qualitatively the various types of interference structures [27–33]. However, since these models assume almost always that a slice through the 3D dynamics is equal to the corresponding 2D dynamics, they are unable to reproduce the positions of the holographic fringes in 3D and the relative weights of various kinds of trajectories. Putting

aside the question of dimensionality, we note that approaches using the semiclassical phase based on Feynman's path integral [31,32] are promising since they lead to the correct number of interference fringes [15,31–34]. Using a glory rescattering model, the shape of the central maximum of the interference pattern was recently described [35–37]. However, without taking interference between different types of trajectories into account, the glory model cannot correctly predict the interference patterns.

In this Letter, we explain quantitatively the interference structures in PMDs by refining the semiclassical description. The central ingredient is the preexponential factor of the semiclassical propagator [38,39] that has been given little attention previously. Its modulus influences strongly the weights of the trajectories. Its phase known as the Maslov phase affects the interference structures. We analyze the focal-point structure of the system and calculate the corresponding Maslov phase which can be identified as a case of Gouy's phase anomaly. For the analysis of the semiclassical trajectories, we propose a method that combines the shooting method [16] with a clustering algorithm to determine all initial momenta that are classically mapped to the given final momenta (inversion problem). This enables us to go beyond [27–31] and to include the correct trajectory weights efficiently.

We begin by calculating PMDs by numerical solution of the TDSE in single-active electron approximation using the split-operator method [37]. In 3D calculations, we choose an effective potential for helium [40] converted into a pseudo-potential for the $1s$ state [41]. In 2D calculations, this potential is further softened by replacing $r \rightarrow \sqrt{r^2 + 0.34}$, providing a 2D helium model with correct ionization potential $I_p \approx 0.9$ a.u. To obtain clean interference structures, we study the ionization dynamics for two-cycle laser pulses as in Ref. [37]. Note, however, that the effects discussed below are also present for longer femtosecond pulses.

The PMDs for pulses polarized linearly along the x axis from solution of the TDSE are shown in Figs. 1(a) and 1(b). Because of the rotational symmetry in 3D, it is sufficient to show a 2D slice at $p_y = 0$. For $p_x < 0$, "direct" non-scattered electrons concentrated along the polarization axis dominate the distributions at momenta below the classical cutoff ($|p_x| \approx 1.63$ a.u.), whereas for $p_x > 0$, holographic fringes roughly parallel to the polarization axis (x axis) are visible. Both regions are overlaid with intracycle interferences roughly parallel to the z axis [15]. The weaker contribution of high-energy electrons, which extends over a large range of momenta p_z (mostly $|p_z| > 0.5$ a.u.), results from hard rescattering [42,43] and exhibits interference rings [44,45]. Even though the 2D and 3D PMDs show the same overall structures, there are obvious differences in the positions of the interference fringes and in the relative strengths of different regions.
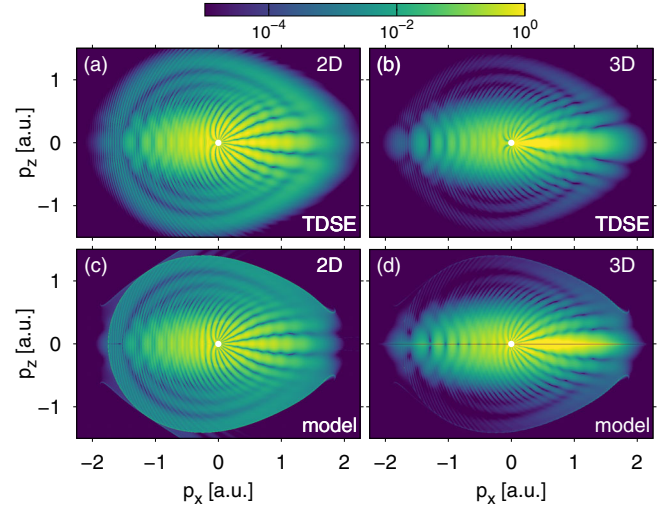

FIG. 1. PMD in 2D [(a),(c)] and a slice along $p_y = 0$ in 3D [(b), (d)] for helium ionized by a two-cycle laser pulse with 4×10^{14} W/cm^2 intensity and 800 nm wavelength. The distributions are calculated by numerical solution of the TDSE in (a),(b) or with the semiclassical model in (c),(d).

Our semiclassical model is based on a combination of strong-field approximation (SFA) in saddle-point approximation (SPA) and semiclassical approximation to the time-dependent propagator formulated as path integral (see Refs. [46,47]) similar to Ref. [32]. We neglect the ionic potential V during the release of an initially bound electron so that this step may be described within the SFA. We introduce connections between initial degrees of freedom such as in Refs. [27–29]: For each initial momentum $\mathbf{p}'$ the possible release times t_0 are given by the real part of the complex-valued SFA saddle-point times $t' = t_0 + it_t$. For its acceleration, the electron starts at the corresponding "tunnel exit" position given by $\mathbf{r}_0 = \text{Re}[\int_{t'}^{t_0} d\tau \mathbf{A}(\tau)]$ with an initial velocity $\dot{\mathbf{r}}_0 = \mathbf{p}' + \mathbf{A}(t_0)$. The dynamics from release time t_0 to final time $t_f \rightarrow \infty$ is modeled by a semiclassical approximation to the mixed position-momentum-space propagator $\langle \mathbf{p}|U(t_f, t_0)|\mathbf{r}_0\rangle$ such that electric field and Coulomb potential are included in a nonperturbative manner. This involves real-valued trajectories satisfying classical equations of motion (EOM) governed by the Hamiltonian $H(\mathbf{r}, \mathbf{p}, t) = \frac{1}{2}[\mathbf{p} + \mathbf{A}(t)]^2 + V(\mathbf{r})$ with the electric field $\mathbf{E}(t) = -\partial_t \mathbf{A}(t)$. As an improvement, complex trajectories can be used [48–50], but we have confirmed that they lead to only minor changes of our observations.

The PMD is proportional to the modulus squared of the transition amplitude which can be approximated in terms of trajectories as (Van Vleck approximation)

$$M_\mathbf{p}(t_f) \propto \sum_s \frac{DC_{\text{Coul}}}{\sqrt{|J(t_f)|}} e^{i(S_\downarrow^0 + S_\rightarrow - \nu\pi/2)}, \quad (1)$$

where s labels all possible initial momenta $\mathbf{p}'$ that are classically mapped to the given final momentum $\mathbf{p}$. The matrix element D is the prefactor from the SFA in SPA, and $C_{\text{Coul}}^2 = [4I_p/|\mathbf{E}(t_0)|]^{2/\sqrt{2I_p}}$ is the Coulomb correction of the ionization rate [27,51,52]. The action associated with each trajectory is split into a complex-valued part corresponding to the ionization step

$$S_{\downarrow}^0 = I_p t' - \int_{t'}^{t_0} dt \frac{[\mathbf{p}' + \mathbf{A}(t)]^2}{2} \qquad (2)$$

and a part corresponding to the acceleration step [31]

$$S_{\rightarrow} = - \int_{t_0}^{\infty} dt \left[\frac{1}{2}\dot{\mathbf{r}}^2(t) + V[\mathbf{r}(t)] - \mathbf{r}(t) \cdot \nabla V[\mathbf{r}(t)] \right]. \qquad (3)$$

The preexponential factor depends on the Jacobian fields $\partial \mathbf{p}(t)/\partial \mathbf{p}'$, $\partial \mathbf{r}(t)/\partial \mathbf{p}'$ [38,39]. These are calculated by integration of the Jacobi initial-value problem [38,53]. The Jacobian J is calculated as

$$J(t) = \det\left(\frac{\partial \mathbf{p}(t)}{\partial \mathbf{p}'} \right). \qquad (4)$$

The Maslov index ν may be viewed as a time-dependent function $\nu(t)$ with $\nu(t_0) = 0$ that can only change at times T with vanishing Jacobian $J(T) = 0$ (focal points). At these points T, there are m linearly independent zero modes $\mathbf{d}^{(i)}$ of $\partial \mathbf{p}(T)/\partial \mathbf{p}'$. Infinitesimal changes of the initial momenta $\mathbf{p}' \to \mathbf{p}' + \epsilon \mathbf{d}^{(i)}$ in these directions $\mathbf{d}^{(i)}$ do not change the momentum $\mathbf{p}(T)$ in first order of ϵ. The corresponding changes $\delta \mathbf{r}^{(i)}$ of the position are

$$\delta \mathbf{r}^{(i)} = \epsilon \sum_j \frac{\partial \mathbf{r}(T)}{\partial p_j'} d_j^{(i)}. \qquad (5)$$

The jump of the Maslov index across focal points is

$$\Delta \nu(T) = m - 1 + \text{sgn} \det(g), \qquad (6)$$

where the matrix elements of the $m \times m$ matrix g are given by $g_{i,j} = \delta \mathbf{r}^{(i)} \cdot \text{Hesse}_{\mathbf{r},\mathbf{r}}(H) \delta \mathbf{r}^{(j)}$ with the Hessian matrix $\text{Hesse}_{\mathbf{r},\mathbf{r}}(H)$ of the Hamiltonian H with respect to positions $\mathbf{r}$ [39]. According to the Morse theorem [54], in position representation $\Delta \nu$ is equal to the multiplicity m. In mixed representation used here, this is not generally true. However, if $\text{Hesse}_{\mathbf{r},\mathbf{r}}(H)$ is positive definite, Eq. (6) reduces to the Morse theorem.

In order to solve the inversion problem, a Monte Carlo algorithm is used to sample the initial momenta $\mathbf{p}'$. The corresponding final momenta $\mathbf{p}$ are binned in cells in momentum space. For a large number $n_{\mathbf{k}}$ of trajectories per bin, the solutions in a single bin form accumulations in the space of initial momenta which may be identified by means of clustering algorithms [55]. Considering vanishing bin sizes, the area covered by the clusters goes to zero and their locations are the solutions of the inversion problem for a final momentum $\mathbf{k}$. This method enables us to determine all possible solutions in a systematic manner, which is a difficult task in other approaches to solving the inversion problem [32]. The area covered by the clusters is proportional to $1/|J|$, so that the shooting methods [16,30,31] imply a wrong weighting of trajectories. Solving the inversion problem allows us to determine the correct weight $1/\sqrt{|J|}$ in Eq. (1).

The PMDs calculated with the semiclassical model for a Coulomb potential $-1/r$ are shown in Figs. 1(c) and 1(d). Our model reproduces the TDSE distributions perfectly as the Jacobian fields depend on the dimension. Using the symmetry in linearly polarized fields, a relation between the Jacobian J_{3D} of the 3D system and the Jacobian J_{2D} of the corresponding 2D system is obtained,

$$|J_{\text{3D}}| = \frac{p_\perp}{p_\perp'} |J_{\text{2D}}| \quad \text{with} \quad p_\perp = \sqrt{p_y^2 + p_z^2}. \qquad (7)$$

This 2D-to-3D correction weight has already been used in Ref. [31]. For direct nonscattered trajectories with $p_\perp \approx p_\perp'$, the Jacobians in both dimensionalities are nearly the same. In contrast, rescattering trajectories with large scattering angles correspond to small initial perpendicular velocity $p_\perp' \ll p_\perp$ such that their Jacobian is enhanced, and hence, their weighting reduced in 3D compared to 2D. Physically, this reflects the increased recollision probability in 2D compared to 3D. Close to the polarization axis, where $p_\perp \approx 0$, the distributions in 3D are greatly enhanced due to Coulomb focusing with $p_\perp' \gg p_\perp$ [26,35]. Hence, the difference in the Jacobian J explains the higher emission strength of electrons with large $p_\perp$ in 2D compared to 3D; see also the different scales of the 1D slices shown in Figs. 2(a)–2(d) and the different modulation depth of the holographic fringes. The longitudinal momentum distributions and especially the positions of intracycle interferences are also well reproduced by the model (not shown).

In 3D, scattered electron wave packets may pass through additional focal points due to Coulomb focusing compared to 2D. Most intuitively, this can be understood in linearly polarized fields. Here, the wave packet is focused (in position space) whenever it crosses the polarization axis, because the rotational symmetry dictates that in such points, all trajectories with the same magnitude of their initial perpendicular velocity and the same release time t_0 are mapped to $r_\perp = 0$. The situation is schematically illustrated in Fig. 3(a). Hence, this quantum-mechanical system is comparable to an optical cylindrical lens creating a line focus with a $\pi/2$ phase shift [56]. We expect another analogy to optics when the semiclassical model is applied to structured vortex electron wave packets which are
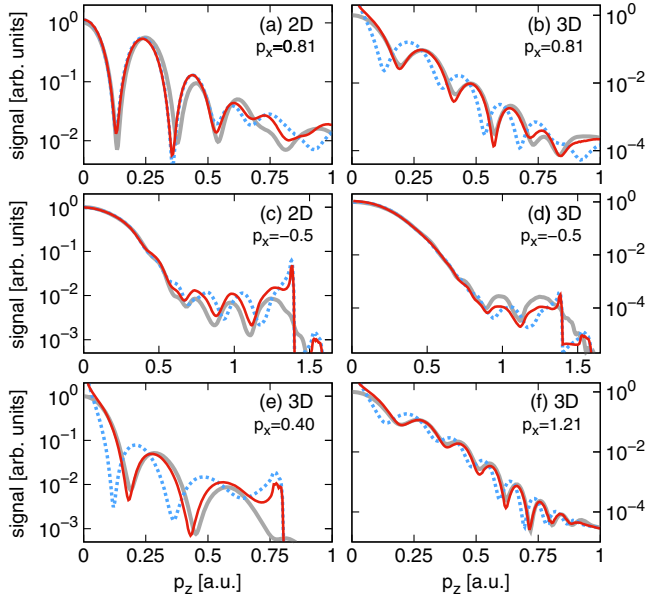
FIG. 2. TDSE results (gray thick lines), semiclassical model including Maslov's phase (red thin lines) or neglecting Maslov's phase (blue dotted lines) for 1D slices through PMDs at fixed p_x. (a)–(d) Parameters as in Fig. 1. In panels (e) and (f) the wavelength dependence is investigated: (e) $\lambda = 400$ nm, (f) $\lambda = 1200$ nm. Calculations in 2D are shown in panels (a), (c). All other panels show 3D data.

formed by strong-field ionization of current-carrying orbitals [57,58].

The Gouy phase anomaly arises from the different Maslov indices in 2D and 3D: For potentials $V(x, r_\perp)$ with a minimum at $r_\perp = 0$ and arbitrary trajectories, it follows from Eq. (6) that the indices are related by

$$\nu_{3D} = \nu_{2D} + \delta\nu, \tag{8}$$

where $\delta\nu$ is the number of zero crossings of $p_\perp(T)$ along the trajectory. The holographic pattern can be understood as
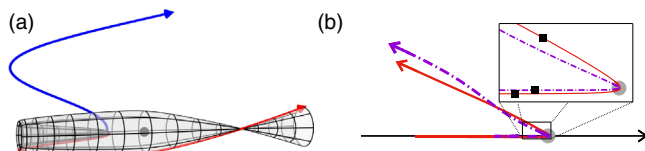

FIG. 3. (a) Photoelectron holography: Interference between the nonscattered trajectory (blue line) and scattered trajectory (red line). Because of the rotational symmetry in 3D, a one-dimensional manifold of trajectories with the same initial perpendicular momentum $p'_\perp$ (indicated as surface) is focused on the polarization axis resulting in a phase shift of $\pi/2$. (b) High-order above-threshold ionization: Interference between long (red solid line) and short (violet dashed-dotted line) rescattering trajectories. The short trajectory passes one focal point (black point) such that the Maslov index $\nu = +1$, whereas the long trajectory passes two focal points (black points) resulting in Maslov index $\nu = 0$.

interference of a nonscattered reference wave and a scattered signal wave [16,24]. For final momenta with $p_y = 0$ and $p_z > 0$, the reference trajectory has a perpendicular initial velocity $p'_z > 0$ and it is only weakly perturbed by the potential. Hence, its Maslov phase is 0. In contrast, the signal trajectory starts with initial velocity $p'_z < 0$, and it is strongly deflected by the potential to its final momentum $p_z > 0$. The calculation shows that the Maslov index in 2D is still 0. However, since in 3D an additional axial focal point is crossed, the Maslov index jumps by 1; see Fig. 3(a). This phase shift affects the positions of minima and maxima for a broad range of wavelengths; see the 1D slices through the holographic "fingers" in Fig. 2.

Holography is also present for non-cylindrically-symmetric laser fields such as bicircular fields consisting of two counterrotating circularly polarized fields with frequencies ω and 2ω [59–61]. Here, in analogy to linear polarization, we find that the central fringe is strongly enhanced, and interference minima are correctly predicted only if Gouy's phase anomaly is taken into account; see Fig. 4. As in linear polarization, these findings are caused by Coulomb focusing of the scattering trajectories with a sign change of their Jacobian. Hence, Coulomb focusing and Gouy phase shifts are not special to (approximately) cylindrically symmetric systems, but rather a general property of scattering trajectories.

There are observable nonvanishing Maslov phases already in 2D. As these phases result from passing through other types of caustics, they have to be calculated numerically using Eq. (6). One example concerns the nearly circular ring structures at high energies arising from interference of short and long rescattering trajectories
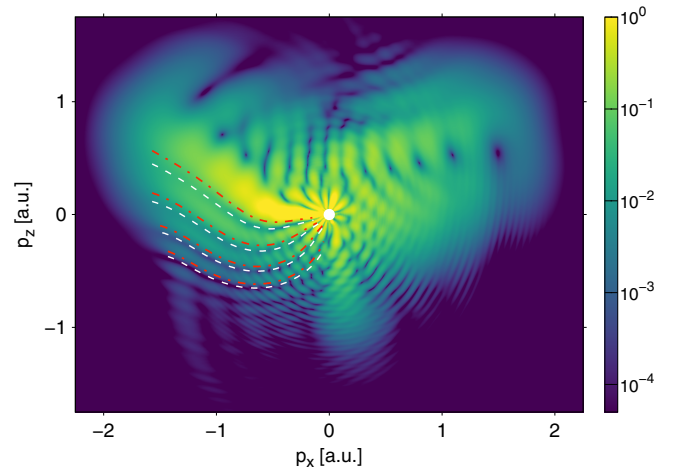

FIG. 4. Slice through the PMD along $p_y = 0$ in 3D for helium ionized by a two-cycle bicircular laser pulse with intensity 8×10^{14} W/cm^2, intensity ratio $I_{2\omega}/I_\omega = 3$, and $\lambda = 800$ nm from numerical solution of the TDSE. The lines mark the positions of the holographic interference minima of the semiclassical model with white dashed lines including Maslov's phase and red dashed-dotted lines neglecting Maslov's phase.

[44,45]. The long trajectory finally reaches $\nu_{2D} = 0$, after passing two focal points in 2D: At one point the Maslov index is increased by $+1$ and at the other it changes by -1. In contrast, the short trajectory only crosses a single focal point in 2D resulting in $\nu_{2D} = +1$; compare Fig. 3(b) for an illustration. The resulting phase difference $\pi/2$ is essential to reproduce the correct positions of the circular ring structures; see the 1D slices in Figs. 2(c) and 2(d). In quantum-orbit models based on the SFA [44,45], this additional phase is automatically included by the Hessian matrix element in the prefactor of the SPA [62].

To conclude, we have shown that Gouy's phase anomaly in electron waves plays a central role in the formation of interference structures in PMDs from strong-field ionization. Coulomb focusing leads to the appearance of focal points for rescattering electrons that are absent in 2D, so that the holographic interference fringes are shifted and the spectral weight is modified. Our quantitative interpretation of the PMDs from atoms by means of a powerful semiclassical model forms the foundation for the future analysis of more complex system with nontrivially polarized fields [60,61,63] or more complex targets such as molecules [22,23,58,64,65]. For the full agreement of our model with *ab initio* TDSE results, the inclusion of preexponential factors is crucial. We have accomplished this task by using an efficient clustering method for solving the inversion problem and have thus shown an alternative approach to resolve one of the problems in the applicability of the Van Vleck propagator. This idea can be transferred to other semiclassically treated problems, e.g., in the context of molecular spectroscopy [53,66,67] or interacting bosons [68], with the advantage of a clearer view on physical processes compared to previously used initial-value representations.

[1] C. R. Gouy, Sur une propriété nouvelle des ondes lumineuses, C.R. Hebd. Seances Acad. Sci. **110**, 1251 (1890).

[2] P. Balcou, P. Salières, A. L'Huillier, and M. Lewenstein, Generalized phase-matching conditions for high harmonics: The role of field-gradient forces, Phys. Rev. A **55**, 3204 (1997).

[3] A. B. Ruffin, J. V. Rudd, J. F. Whitaker, S. Feng, and H. G. Winful, Direct Observation of the Gouy Phase Shift with Single-Cycle Terahertz Pulses, Phys. Rev. Lett. **83**, 3410 (1999).

[4] F. Lindner, G. G. Paulus, H. Walther, A. Baltuška, E. Goulielmakis, M. Lezius, and F. Krausz, Gouy Phase Shift for Few-Cycle Laser Pulses, Phys. Rev. Lett. **92**, 113001 (2004).

[5] E. R. Andresen, C. Finot, D. Oron, and H. Rigneault, Spectral Analog of the Gouy Phase Shift, Phys. Rev. Lett. **110**, 143902 (2013).

[6] N. C. R. Holme, B. C. Daly, M. T. Myaing, and T. B. Norris, Gouy phase shift of single-cycle picosecond acoustic pulses, Appl. Phys. Lett. **83**, 392 (2003).

[7] C. R. Carpenter, Gouy phase advance with microwaves, Am. J. Phys. **27**, 98 (1959).

[8] T. Feurer, N. S. Stoyanov, D. W. Ward, and K. A. Nelson, Direct Visualization of the Gouy Phase by Focusing Phonon Polaritons, Phys. Rev. Lett. **88**, 257402 (2002).

[9] I. G. da Paz, P. L. Saldanha, M. C. Nemes, and J. G. P. de Faria, Experimental proposal for measuring the Gouy phase of matter waves, New J. Phys. **13**, 125005 (2011).

[10] G. Guzzinati, P. Schattschneider, K. Y. Bliokh, F. Nori, and J. Verbeeck, Observation of the Larmor and Gouy Rotations with Electron Vortex Beams, Phys. Rev. Lett. **110**, 093601 (2013).

[11] T. C. Petersen, D. M. Paganin, M. Weyland, T. P. Simula, S. A. Eastwood, and M. J. Morgan, Measurement of the Gouy phase anomaly for electron waves, Phys. Rev. A **88**, 043803 (2013).

[12] T. F. Gallagher, Above-Threshold Ionization in Low-Frequency Limit, Phys. Rev. Lett. **61**, 2304 (1988).

[13] P. B. Corkum, N. H. Burnett, and F. Brunel, Above-Threshold Ionization in the Long-Wavelength Limit, Phys. Rev. Lett. **62**, 1259 (1989).

[14] F. Lindner, M. G. Schätzel, H. Walther, A. Baltuška, E. Goulielmakis, F. Krausz, D. B. Milošević, D. Bauer, W. Becker, and G. G. Paulus, Attosecond Double-Slit Experiment, Phys. Rev. Lett. **95**, 040401 (2005).

[15] R. Gopal, K. Simeonidis, R. Moshammer, Th. Ergler, M. Dürr, M. Kurka, K.-U. Kühnel, S. Tschuch, C.-D. Schröter, D. Bauer, J. Ullrich, A. Rudenko, O. Herrwerth, Th. Uphues, M. Schultze, E. Goulielmakis, M. Uiberacker, M. Lezius, and M. F. Kling, Three-Dimensional Momentum Imaging of Electron Wave Packet Interference in Few-Cycle Laser Pulses, Phys. Rev. Lett. **103**, 053001 (2009).

[16] Y. Huismans *et al.*, Time-resolved holography with photoelectrons, Science **331**, 61 (2011).

[17] Ph. A. Korneev, S. V. Popruzhenko, S. P. Goreslavski, T.-M. Yan, D. Bauer, W. Becker, M. Kübel, M. F. Kling, C. Rödel, M. Wünsche, and G. G. Paulus, Interference Carpets in Above-Threshold Ionization: From the Coulomb-Free to the Coulomb-Dominated Regime, Phys. Rev. Lett. **108**, 223601 (2012).

[18] X. Xie, S. Roither, D. Kartashov, E. Persson, D. G. Arbó, L. Zhang, S. Gräfe, M. S. Schöffler, J. Burgdörfer, A. Baltuška, and M. Kitzler, Attosecond Probe of Valence-Electron Wave Packets by Subcycle Sculpted Laser Fields, Phys. Rev. Lett. **108**, 193004 (2012).

[19] D. Gabor, in *Nobel Lectures, Physics* (World Scientific, Singapore, 1992), pp. 1971–1980.

[20] Y. Huismans, A. Gijsbertsen, A. S. Smolkowska, J. H. Jungmann, A. Rouzée, P. S. W. M. Logman, F. Lépine, C. Cauchy, S. Zamith, T. Marchenko, J. M. Bakker, G. Berden, B. Redlich, A. F. G. van der Meer, M. Yu. Ivanov, T.-M. Yan, D. Bauer, O. Smirnova, and M. J. J. Vrakking, Scaling Laws for Photoelectron Holography in the Midinfrared Wavelength Regime, Phys. Rev. Lett. **109**, 013002 (2012).

[21] M. Meckel, A. Staudte, S. Patchkovskii, D. M. Villeneuve, P. B. Corkum, R. Dörner, and M. Spanner, Signatures of the continuum electron phase in molecular strong-field photoelectron holography, Nat. Phys. **10**, 594 (2014).

[22] M. Haertelt, X.-B. Bian, M. Spanner, A. Staudte, and P. B. Corkum, Probing Molecular Dynamics by Laser-Induced Backscattering Holography, Phys. Rev. Lett. **116**, 133001 (2016).

[23] S. G. Walt, N. Bhargava Ram, M. Atala, N. I. Shvetsov-Shilovski, A. von Conta, D. Baykusheva, M. Lein, and H. J. Wörner, Dynamics of valence-shell electrons and nuclei probed by strong-field holography and rescattering, Nat. Commun. **8**, 15651 (2017).

[24] X.-B. Bian, Y. Huismans, O. Smirnova, K. J. Yuan, M. J. J. Vrakking, and A. D. Bandrauk, Subcycle interference dynamics of time-resolved photoelectron holography with midinfrared laser pulses, Phys. Rev. A **84**, 043420 (2011).

[25] X.-B. Bian and A. D. Bandrauk, Attosecond Time-Resolved Imaging of Molecular Structure by Photoelectron Holography, Phys. Rev. Lett. **108**, 263003 (2012).

[26] T. Brabec, M. Yu. Ivanov, and P. B. Corkum, Coulomb focusing in intense field atomic processes, Phys. Rev. A **54**, R2551 (1996).

[27] S. V. Popruzhenko and D. Bauer, Strong field approximation for systems with Coulomb interaction, J. Mod. Opt. **55**, 2573 (2008).

[28] S. V. Popruzhenko, G. G. Paulus, and D. Bauer, Coulomb-corrected quantum trajectories in strong-field ionization, Phys. Rev. A **77**, 053409 (2008).

[29] T.-M. Yan, S. V. Popruzhenko, M. J. J. Vrakking, and D. Bauer, Low-Energy Structures in Strong Field Ionization Revealed by Quantum Orbits, Phys. Rev. Lett. **105**, 253002 (2010).

[30] M. Li, J.-W. Geng, H. Liu, Y. Deng, C. Wu, L.-Y. Peng, Q. Gong, and Y. Liu, Classical-Quantum Correspondence for Above-Threshold Ionization, Phys. Rev. Lett. **112**, 113002 (2014).

[31] N. I. Shvetsov-Shilovski, M. Lein, L. B. Madsen, E. Räsänen, C. Lemell, J. Burgdörfer, D. G. Arbó, and K. Tőkési, Semiclassical two-step model for strong-field ionization, Phys. Rev. A **94**, 013415 (2016).

[32] X.-Y. Lai, C. Poli, H. Schomerus, and C. Figueira de Morisson Faria, Influence of the Coulomb potential on above-threshold ionization: A quantum-orbit analysis beyond the strong-field approximation, Phys. Rev. A **92**, 043407 (2015).

[33] D. G. Arbó, E. Persson, and J. Burgdörfer, Time double-slit interferences in strong-field tunneling ionization, Phys. Rev. A **74**, 063407 (2006).

[34] D. G. Arbó, S. Yoshida, E. Persson, K. I. Dimitriou, and J. Burgdörfer, Interference Oscillations in the Angular Distribution of Laser-Ionized Electrons Near Ionization Threshold, Phys. Rev. Lett. **96**, 143003 (2006).

[35] Q. Z. Xia, J. F. Tao, J. Cai, L. B. Fu, and J. Liu, Quantum Interference of Glory Rescattering in Strong-Field Atomic Ionization, Phys. Rev. Lett. **121**, 143201 (2018).

[36] S. D. López and D. G. Arbó, Holographic interference in atomic photoionization from a semiclassical standpoint, Phys. Rev. A **100**, 023419 (2019).

[37] S. Brennecke and M. Lein, Strong-field photoelectron holography beyond the electric dipole approximation: A semiclassical analysis, Phys. Rev. A **100**, 023413 (2019).

[38] S. Levit and U. Smilansky, The Hamiltonian path integrals and the uniform semiclassical approximations for the propagator, Ann. Phys. (N.Y.) **108**, 165 (1977).

[39] S. Levit, K. Möhring, U. Smilansky, and T. Dreyfus, Focal points and the phase of the semiclassical propagator, Ann. Phys. (N.Y.) **114**, 223 (1978).

[40] X. M. Tong and C. D. Lin, Empirical formula for static field ionization rates of atoms and molecules by lasers in the barrier-suppression regime, J. Phys. B **38**, 2593 (2005).

[41] N. Troullier and J. L. Martins, Efficient pseudopotentials for plane-wave calculations, Phys. Rev. B **43**, 1993 (1991).

[42] G. G. Paulus, W. Becker, W. Nicklich, and H. Walther, Rescattering effects in above-threshold ionization: A classical model, J. Phys. B **27**, L703 (1994).

[43] G. G. Paulus, W. Nicklich, H. Xu, P. Lambropoulos, and H. Walther, Plateau in above Threshold Ionization Spectra, Phys. Rev. Lett. **72**, 2851 (1994).

[44] G. G. Paulus, F. Grasbon, A. Dreischuh, H. Walther, R. Kopold, and W. Becker, Above-Threshold Ionization by an Elliptically Polarized Field: Interplay Between Electronic Quantum Trajectories, Phys. Rev. Lett. **84**, 3791 (2000).

[45] R. Kopold, D. B. Milošević, and W. Becker, Rescattering Processes for Elliptical Polarization: A Quantum Trajectory Analysis, Phys. Rev. Lett. **84**, 3831 (2000).

[46] F. Grossmann, *Theoretical Femtosecond Physics: Atoms and Molecules in Strong Laser Fields* (Springer, New York, 2008).

[47] H. Kleinert, *Path Integrals in Quantum Mechanics, Statistics, Polymer Physics, and Financial Markets* (World Scientific, Singapore, 2009).

[48] L. Torlina, J. Kaushal, and O. Smirnova, Time-resolving electron-core dynamics during strong-field ionization in circularly polarized fields, Phys. Rev. A **88**, 053403 (2013).

[49] E. Pisanty and M. Ivanov, Slalom in complex time: Emergence of low-energy structures in tunnel ionization via complex-time contours, Phys. Rev. A **93**, 043408 (2016).

[50] A. S. Maxwell, S. V. Popruzhenko, and C. Figueira de Morisson Faria, Treating branch cuts in quantum trajectory models for photoelectron holography, Phys. Rev. A **98**, 063423 (2018).

[51] A. M. Perelomov and V. S. Popov, Ionization of atoms in an alternating electrical field. III, Sov. Phys. JETP **25**, 336 (1967).

[52] C. Z. Bisgaard and L. B. Madsen, Tunneling ionization of atoms, Am. J. Phys. **72**, 249 (2004).

[53] K. G. Kay, Semiclassical propagation for multidimensional systems by an initial value method, J. Chem. Phys. **101**, 2250 (1994).

[54] M. Morse, *Variational Analysis* (Wiley, New York, 1973).

[55] We use density-based spatial clustering of applications with noise algorithms.

[56] R. W. McGowan, R. A. Cheville, and D. Grischkowsky, Direct observation of the Gouy phase shift in THz impulse ranging, Appl. Phys. Lett. **76**, 670 (2000).

[57] S. M. Baumann, D. M. Kalb, L. H. MacMillan, and E. J. Galvez, Propagation dynamics of optical vortices due to Gouy phase, Opt. Express **17**, 9818 (2009).

[58] O. I. Tolstikhin and T. Morishita, Strong-field ionization, rescattering, and target structure imaging with vortex electrons, Phys. Rev. A **99**, 063415 (2019).

[59] D. B. Milošević and W. Becker, Improved strong-field approximation and quantum-orbit theory: Application to ionization by a bicircular laser field, Phys. Rev. A **93**, 063418 (2016).

[60] S. Eckart, M. Kunitski, I. Ivanov, M. Richter, K. Fehre, A. Hartung, J. Rist, K. Henrichs, D. Trabert, N. Schlott, L. Ph. H. Schmidt, T. Jahnke, M. S. Schöffler, A. Kheifets, and R. Dörner, Subcycle interference upon tunnel ionization by counter-rotating two-color fields, Phys. Rev. A **97**, 041402(R) (2018).

[61] M. Li, W.-C. Jiang, H. Xie, S. Luo, Y. Zhou, and P. Lu, Strong-field photoelectron holography of atoms by bicircular two-color laser pulses, Phys. Rev. A **97**, 023415 (2018).

[62] S. Brennecke and M. Lein, High-order above-threshold ionization beyond the electric dipole approximation: Dependence on the atomic and molecular structure, Phys. Rev. A **98**, 063414 (2018).

[63] C. A. Mancuso, D. D. Hickstein, K. M. Dorney, J. L. Ellis, E. Hasović, R. Knut, P. Grychtol, C. Gentry, M. Gopalakrishnan, D. Zusin, F. J. Dollar, X.-M. Tong, D. B. Milošević, W. Becker, H. C. Kapteyn, and M. M. Murnane, Controlling electron-ion rescattering in two-color circularly polarized femtosecond laser fields, Phys. Rev. A **93**, 053406 (2016).

[64] K. Doblhoff-Dier, K. I. Dimitriou, A. Staudte, and S. Gräfe, Classical analysis of Coulomb effects in strong-field ionization of H_2^+ by intense circularly polarized laser fields, Phys. Rev. A **88**, 033411 (2013).

[65] M.-M. Liu, M. Li, C. Wu, Q. Gong, A. Staudte, and Y. Liu, Phase Structure of Strong-Field Tunneling Wave Packets from Molecules, Phys. Rev. Lett. **116**, 163004 (2016).

[66] K. G. Kay, Semiclassical initial value treatments of atoms and molecules, Annu. Rev. Phys. Chem. **56**, 255 (2005).

[67] R. Conte, F. Gabas, G. Botti, Y. Zhuang, and M. Ceotto, Semiclassical vibrational spectroscopy with Hessian databases, J. Chem. Phys. **150**, 244118 (2019).

[68] S. Ray, P. Ostmann, L. Simon, F. Grossmann, and W. T. Strunz, Dynamics of interacting bosons using the Herman-Kluk semiclassical initial value representation, J. Phys. A **49**, 165303 (2016).